



CHORUS

This is the accepted manuscript made available via CHORUS. The article has been published as:

Frequency Combs in a Lumped-Element Josephson-Junction Circuit

Saeed Khan and Hakan E. Türeci

Phys. Rev. Lett. **120**, 153601 — Published 9 April 2018

DOI: [10.1103/PhysRevLett.120.153601](https://doi.org/10.1103/PhysRevLett.120.153601)

Frequency combs in a lumped element Josephson junction circuit

S. Khan and H. E. Türeci

Department of Electrical Engineering, Princeton University, Princeton, New Jersey 08544, USA

(Dated: March 1, 2018)

We investigate the dynamics of a microwave-driven Josephson junction capacitively coupled to a lumped element LC oscillator. In the regime of driving where the Josephson junction can be approximated as a Kerr oscillator, this minimal nonlinear system has been previously shown to exhibit a bistability in phase and amplitude. In the present study, we characterize the full phase diagram and show that besides a parameter regime exhibiting bistability, there is also a regime of self-oscillations characterized by a frequency comb in its spectrum. We discuss the mechanism of comb generation which appears to be different from those studied in microcavity frequency combs and mode-locked lasers. We then address the fate of the comb-like spectrum in the regime of strong quantum fluctuations, reached when nonlinearity becomes the dominant scale with respect to dissipation. We find that the nonlinearity responsible for the emergence of the frequency combs also leads to its dephasing, leading to broadening and ultimate disappearance of sharp spectral peaks. Our study explores the fundamental question of the impact of quantum fluctuations for quantum systems which do not possess a stable fixed point in the classical limit.

In superconducting quantum circuits, the Josephson junction (JJ) is a lossless nonlinear element that provides critical functionality for various quantum information processing tasks [1–3], from gate operations to readout and amplification, made possible by controlling JJ dynamics via its embedding circuit and effective drive. For instance, under strong coupling and weak excitation (relative to the intrinsic nonlinearity), JJ-based artificial atoms have enabled Cavity QED implementations [4–9] that have been extensively discussed using open Jaynes-Cummings or Rabi models in single [10] and multi-mode regimes [11]. However, applications employing JJs under strong excitation conditions, for readout [12–14] and quantum-limited amplification [15–19], require an understanding of dynamical instabilities that sensitively depend on the model of nonlinearity employed [20, 21].

Here we investigate the dynamics of a shunted JJ when capacitively coupled to a microwave-driven linear resonator. The dynamics of such a system under strong driving have been theoretically [10, 22] and experimentally [12] studied in the context of a high-power read-out scheme, and are found to exhibit a bistability between two states with distinct phase and amplitude. In the adiabatic regime where mode coupling is weaker than losses, the coupled system maps to a single coherently-driven Kerr oscillator with renormalized parameters, exhibiting precisely this bistability [13, 23–25]. However, we find that in the strong-coupling regime the nonlinear mode acquires a retarded self-interaction mediated by the linear mode, which changes the classical phase diagram dramatically: for certain drive and detuning ranges the system may have *no* stable fixed points, a phase not exhibited by the single coherently-driven Kerr oscillator [26]. In this dynamical regime, nonzero frequency instabilities emerge as limit cycles, yielding discrete, equally spaced comb-like spectra in the frequency domain.

Such comb formation in coherently-driven microresonators [27–31] and incoherently-pumped mode-locked lasers [32, 33] is often understood as an instability towards symmetric sideband growth via four-wave mixing, in an underlying resonator geometry supporting multiple spatial modes [36, 37]

and a distributed nonlinearity (while exceptions have been discussed as well [34, 35, 38]). Our results indicate that the minimal manifestation of Kerr-mediated comb formation is embodied in a Kerr-oscillator coupled to a linear oscillator.

While limit cycles [39, 40] and their modification under classical noise [38, 41] have been extensively studied in classical systems, they are far less explored in the deep quantum regime [42, 43] accessible to the lumped element JJ circuit discussed here. Using Master equation and phase-space simulations, we investigate the fate of comb-like spectra as the nonlinearity is tuned from weak to strong (equivalently, high to low mode occupation at the instability threshold), so that the system moves from an expected semiclassical regime towards a well-defined quantum regime where a single photon can in principle trigger the comb instability. We find that while the nonlinearity, together with strong enough coupling to the linear mode, is necessary for limit cycles to emerge, this very nonlinearity introduces quantum noise that dephases the limit cycle; for weak noise, the dephasing time typically scales inversely with the strength of the nonlinearity.

Model - The model we study is realizable in lumped element setups [Fig. 1 (c)], as well as JJ-embedded transmission-line resonators [44]. We assume that the nonlinearity of the junction can be approximated by its lowest order Kerr nonlinearity. The resulting model described by the Hamiltonian $\hat{\mathcal{H}} = \hat{\mathcal{H}}_a + \hat{\mathcal{H}}_b + \hat{\mathcal{H}}_g + \hat{\mathcal{H}}_d$ (See SM [45]) then is generic, consisting of a driven linear oscillator a (frequency ω_a) coupled to a nonlinear

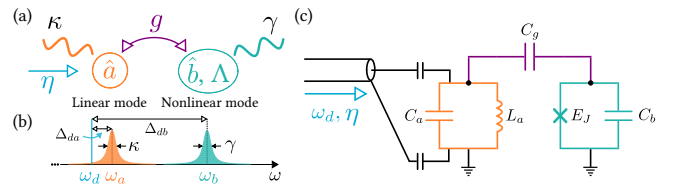


Figure 1. (a) Schematic representation of the two-mode system. (b) Mode and drive frequencies. (c) Lumped element circuit QED implementation of (a).

oscillator b (frequency ω_b) [Fig. 1 (a)]. $\hat{\mathcal{H}}_d = \eta(\hat{a} + \hat{a}^\dagger)$ describes the drive (strength η) in the frame rotating at the drive frequency ω_d . The corresponding drive frame Hamiltonians of the modes are $\hat{\mathcal{H}}_a = -\Delta_{da}\hat{a}^\dagger\hat{a}$ and $\hat{\mathcal{H}}_b = -\Delta_{db}\hat{b}^\dagger\hat{b} - \frac{\Lambda}{2}\hat{b}^\dagger\hat{b}^\dagger\hat{b}\hat{b}$ respectively, with $\Lambda > 0$ being the strength of the nonlinearity, and the frequency detunings defined as $\Delta_{da/db} = \omega_d - \omega_{a/b}$. The two oscillators are coupled linearly, with Hamiltonian $\hat{\mathcal{H}}_g = g(\hat{a}^\dagger\hat{b} + \hat{b}^\dagger\hat{a})$. The system dynamics including damping for both the linear (rate κ) and nonlinear mode (rate γ) are then governed by the Master equation $\dot{\hat{\rho}} = -i[\mathcal{H}, \hat{\rho}] + \kappa\mathcal{D}[\hat{a}]\hat{\rho} + \gamma\mathcal{D}[\hat{b}]\hat{\rho}$, where $\mathcal{D}[\hat{o}]$ is the standard dissipative superoperator $\mathcal{D}[\hat{o}]\rho = \hat{o}\rho\hat{o}^\dagger - \frac{1}{2}\{\hat{o}^\dagger\hat{o}, \rho\}$.

We begin with the classical dynamics of the two-mode system, obtaining operator equations of motion and making the replacement $(\langle\hat{a}\rangle, \langle\hat{b}\rangle) \rightarrow (\alpha, \beta)$. This yields:

$$\dot{\alpha} = i\Delta_{da}\alpha - \frac{\kappa}{2}\alpha - ig\beta - i\eta; \quad \dot{\beta} = i\Delta_{db}\beta - \frac{\gamma}{2}\beta + i\Lambda|\beta|^2\beta - ig\alpha \quad (1)$$

Note that Eqs. (1) are invariant if $\Lambda \rightarrow \Lambda/c$ and $(\alpha, \beta, \eta) \rightarrow \sqrt{c}(\alpha, \beta, \eta)$, for $c \in \mathbb{R}^+$ [45]. Physically, scaling $\Lambda \rightarrow \Lambda/c$ and $\eta \rightarrow \sqrt{c}\eta$ yields the same *classical* dynamics, except with mode amplitudes scaled by \sqrt{c} . This simple Λ -dependence is not true of the *quantum* dynamics, as we shall see later. Next, the linearity of mode \hat{a} and the coupling allows it to be integrated out exactly, leading to an effective dynamical equation for the nonlinear mode:

$$\dot{\beta} = i\Delta_{db}\beta - \frac{\gamma}{2}\beta + i\Lambda|\beta|^2\beta + g\chi_a\eta \left[e^{(i\Delta_{da} - \frac{\kappa}{2})t} - 1 \right] - g^2 \int_0^t d\tau F(\tau)\beta(t - \tau), \quad (2)$$

where the linear mode susceptibility $\chi_a^{-1} = -i\Delta_{da} + \kappa/2$. **The first line is** the classical equation of motion for a coherently-driven Kerr oscillator; the drive term is $\propto g\chi_a$ since the linear mode is driven. More interesting is the term in the second line, which describes the delayed self-interaction of the nonlinear mode - mediated by the linear mode - with a memory kernel $F(\tau) = e^{(i\Delta_{da} - \frac{\kappa}{2})\tau}$.

When $F(\tau)$ decays rapidly relative to the timescale of system dynamics ($\kappa \gg g$), we may set $\beta(t - \tau) \approx \beta(t)$ within a Markov approximation; this is also equivalent to adiabatically eliminating the linear mode ($\dot{\alpha} \approx 0$). We then obtain an effective Markov regime equation for the (long-time) dynamics of the nonlinear mode:

$$\dot{\beta} = i\tilde{\Delta}_{db}\beta - \frac{\tilde{\gamma}}{2}\beta + i\Lambda|\beta|^2\beta - \tilde{\eta} \quad (3)$$

This is the classical dynamical equation for a renormalized Kerr oscillator, with modified detuning $\tilde{\Delta}_{db} = \omega_d - (\omega_b + g^2\Delta_{da}|\chi_a|^2)$, damping $\tilde{\gamma} = \gamma + g^2\kappa|\chi_a|^2$ and drive $\tilde{\eta} = g\chi_a\eta$. Therefore, when the linear mode can be adiabatically eliminated, the two-mode system behaves like an effective Kerr oscillator [46].

From here, the classical fixed points $(\bar{\alpha}, \bar{\beta})$ of the two-mode system are found by setting $\dot{\alpha} = \dot{\beta} = 0$, or equivalently setting $\dot{\beta} = 0$ in the Markov regime equation, Eq. (3). The

equation relating the fixed points $|\bar{\beta}|^2$ to the drive strength $|\eta|^2$ is found to be the standard cubic polynomial for a Kerr oscillator, with the modified parameters defined earlier [45]. The relationship is single-valued for $\Delta_{db} > \Delta_{db}^{\text{MP}}$ but becomes multivalued for $\Delta_{db} < \Delta_{db}^{\text{MP}}$, defining a region of multiple fixed points; here the critical detuning $\Delta_{db}^{\text{MP}} = -\frac{\sqrt{3}}{2}(\gamma + g^2\kappa|\chi_a|^2) + g^2\Delta_{da}|\chi_a|^2$ [45]. Dropping terms $\propto g^2$ arising from the linear mode yields the standard result for a single driven Kerr oscillator.

Stability analysis - To treat the memory term exactly we perform a Laplace domain linear stability analysis around the above fixed points; details can be found in [45]. Instability is determined by the dominant pole (pole with largest real part) of the linearized dynamical matrix. For a resonantly driven linear mode, $\Delta_{da} = 0$, an analysis of the real and imaginary parts of the poles separately allows the phase diagram to be mapped out entirely analytically; we focus on this case from here on (for non-zero Δ_{da} , see SM [45]). Two distinct parameter regimes are obtained, determined by the relative strength of g and κ .

For $g < \kappa/2$, the typical phase diagram in η - Δ_{db} space is shown in Fig. 2 (a). For $\Delta_{db} > \Delta_{db}^{\text{MP}}$, the system has only one fixed point (FP), as discussed earlier; the stability analysis indicates that this FP is always stable. For $\Delta_{db} < \Delta_{db}^{\text{MP}}$, the orange hatched region emerges where one of the system's FPs is unstable, and the unstable pole s has $\text{Im } s = 0$. In this region, the typical curve relating $|\bar{\beta}|^2$ to η (S-curve) is shown in the inset, with green (purple) segments showing unstable (stable) FPs. The unstable FPs coincide *exactly* with the region of 3 total FPs; dynamically, instabilities from the unstable branch settle into one of the two stable fixed points at the same drive strength. This is precisely the stability diagram of the modified Kerr oscillator defined by Eq. (3).

Much more interesting is the case $g > \kappa/2$, for which the phase diagram is shown in Fig. 2 (b). We first consider $\Delta_{db} > \Delta_{db}^{\text{MP}}$, where the classical equations admit only 1 FP. We find that for Δ_{db} above a minimum critical detuning $\Delta_{db}^{\text{LC}} = -\frac{\sqrt{3}}{2}(\gamma + \kappa)$, the single fixed point that exists is never unstable (region 1). For $\Delta_{db}^{\text{MP}} < \Delta_{db} < \Delta_{db}^{\text{LC}}$ (region 2), this is no longer the case. A typical $|\bar{\beta}|^2$ - η plot in region 2, Fig. 2 (c), shows emergent unstable $|\bar{\beta}|^2$ values in green, where the system has only one, *unstable* FP, hinting at the emergence of limit cycle solutions; this regime is not possible for the single coherently-driven Kerr oscillator. The *minimum* and *maximum unstable* $|\bar{\beta}|^2$ values occur at drive strengths η_- (open square) and η_+ (filled circle) respectively. At these drives, the dominant pole reaches the threshold of instability, now with nonzero $\text{Im } s = \pm\sqrt{g^2 - \kappa^2/4} \equiv \pm\Omega$.

Note that for $\eta > \eta_+$ and $\eta < \eta_-$, the system always has at least one stable fixed point (lying on one of the upward pointing purple segments). Also, in region 2, the unstable green segments lie entirely in the drive range $\eta_- < \eta < \eta_+$. However, with more negative detuning, the latter does not remain so. For $\Delta_{db} < \Delta_{db}^{\text{MP}}$ (regions 3, 4), the S-curve can be multivalued, as seen in Fig. 2 (d), and eventually further deforms to Fig. 2 (e), where unstable $|\bar{\beta}|^2$ are *not* all contained

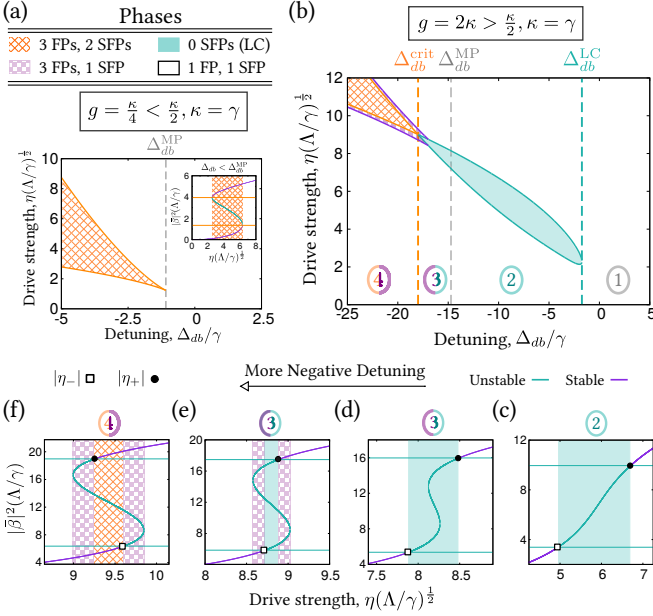


Figure 2. Phase diagram in η - Δ_{db} space. The possible phases are listed in the top-left table. (a) Phase diagram for $g < \frac{\kappa}{2}$ (here, $g = \frac{\kappa}{4}$). (b) Phase diagram for $g > \frac{\kappa}{2}$ (here, $g = 2\kappa$). (c) through (f) Plots of $|\bar{\beta}|^2$ against η showing the change in the S-curve as Δ_{db} is swept across the four dynamical regions in (b). Green (purple) segments of the S-curve depict unstable (stable) $|\bar{\beta}|^2$ values.

in the range $\eta_- < \eta < \eta_+$. Here, for $\eta > \eta_+$ and $\eta < \eta_-$ the system now admits 3 FPs, of which *only one* is stable (checked purple). On the other hand, *within* the range $\eta_- < \eta < \eta_+$ (shaded green as before), *all three fixed points are unstable*. This is clearly seen in Fig. 2 (e): only green segments of the S-curve lie in the green shaded region.

Furthermore, the range $\eta_- < \eta < \eta_+$ is detuning dependent; as Δ_{db} becomes more negative, this region shrinks, and vanishes when $\eta_- = \eta_+$. We mark this as the terminal boundary of region 3, which occurs at a critical detuning $\Delta_{db}^{\text{crit}} = -\sqrt{(\Delta_{db}^{\text{MP}})^2 + \frac{1}{2}[(\Delta_{db}^{\text{MP}})^2 - (\Delta_{db}^{\text{LC}})^2]}$ [dashed orange line in Fig. 2 (b)].

For $\Delta_{db} < \Delta_{db}^{\text{crit}}$, region 4 begins, where $\eta_- > \eta_+$. The S-curve typically looks like Fig. 2 (f). Since at least one stable fixed point always exists for $\eta > \eta_+$ and $\eta < \eta_-$, and since $\eta_- > \eta_+$ in region 4, we easily conclude that at least one *stable* fixed point (SFP) now exists for *all* driving strengths. The green shaded region with 0 SFPs thus gives way to the orange hatched region with 3 FPs, 2 SFPs. We note that unlike Δ_{db}^{LC} , which is a strict minimal detuning for instability, $\Delta_{db}^{\text{crit}}$ is *not* a strict *maximal* detuning. Beyond $\Delta_{db}^{\text{crit}}$, limit cycle solutions can ostensibly still emerge, since unstable fixed points with nonzero $\text{Im } s$ still exist. However, if excursions from these unstable fixed points are large enough, the system can always find a stable fixed point to settle into in this region.

Finally, as $g \rightarrow \kappa/2$, $\Delta_{db}^{\text{crit}}$, Δ_{db}^{MP} , Δ_{db}^{LC} all become equal; both green and purple regions shrink and eventually vanish, such that for $g < \kappa/2$, only the orange hatched region persists,

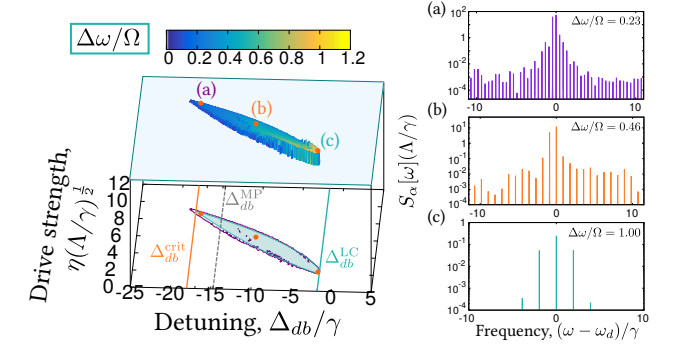


Figure 3. Numerically simulated phase diagram in η - Δ_{db} space for $g = 2\kappa > \frac{\kappa}{2}$. Surface plot shows spectral spacing $\Delta\omega$ obtained from $S_\alpha[\omega]$; the ‘island’ of multifrequency solutions overlaps perfectly with the analytically-predicted unstable region below (shaded green). Plots (a) through (c) show $S_\alpha[\omega]$ at the correspondingly labelled points on the phase diagram.

and we recover the phase diagram in Fig. 2 (a).

Dynamics in the unstable region can be studied numerically by simulating Eqs. (1). We calculate the steady state power spectrum of the linear mode, $S_\alpha[\omega] = |\mathcal{F}\{\alpha(t)\}|^2$, where $\mathcal{F}\{\alpha(\tau)\} = \int_{-\infty}^{\infty} d\tau e^{-i\omega\tau}\alpha(\tau)$ is the Fourier transform. This quantity is of particular relevance for circuit QED realizations of our model, where $S_\alpha[\omega]$ is the power spectrum of the resonator mode, which can be directly monitored in experiments [47]. For each spectrum $S_\alpha[\omega]$, the frequency spacing $\Delta\omega$ is plotted in η - Δ_{db} space in Fig. 3, scaled by Ω . We find multifrequency limit cycles in a region that has excellent agreement with the (green shaded) analytic region of 0 SFPs. The spacing $\Delta\omega$ is close to Ω for $\Delta_{db} \sim \Delta_{db}^{\text{LC}}$, but decreases as Δ_{db} becomes more negative; this reduction is observed for general parameters in this system (see additional phase diagrams included in [45]).

Quantum regime - To study the modification of limit cycle dynamics in the quantum regime, we employ both Master equation simulations and a stochastic approach based on the positive- P representation of the density matrix ρ [48]. The latter allows access to normal-ordered operator averages and correlation functions via a set of stochastic differential equations (SDEs) for the independent complex variables $\vec{\alpha} \equiv (\alpha, \alpha^\dagger, \beta, \beta^\dagger)$:

$$d\vec{\alpha} = \vec{A} dt + \sqrt{\Lambda} \mathbf{B} d\vec{W} \quad (4)$$

The drift vector \vec{A} describes deterministic classical evolution, equivalent to Eqs. (1). Then, by construction, any quantum effects must appear as stochastic ‘noise’ terms, involving the vector of independent Wiener increments $d\vec{W}$. The scale and nature of this noise is set by the matrix \mathbf{B} . In the absence of thermal noise (which we neglect), $\mathbf{B} = \sqrt{i} \text{diag}(0, 0, \beta, i\beta^\dagger)$ is purely quantum in origin, and depends on β, β^\dagger (as opposed to being constant for thermal noise). Eqs. (4) are thus driven by *multiplicative* noise. Crucially, the classical and quantum contributions depend differently on the nonlinearity. Scaling $\Lambda \rightarrow \Lambda/c$ and $(\vec{\alpha}, \eta) \rightarrow \sqrt{c}(\vec{\alpha}, \eta)$ in Eqs. (4) leaves the

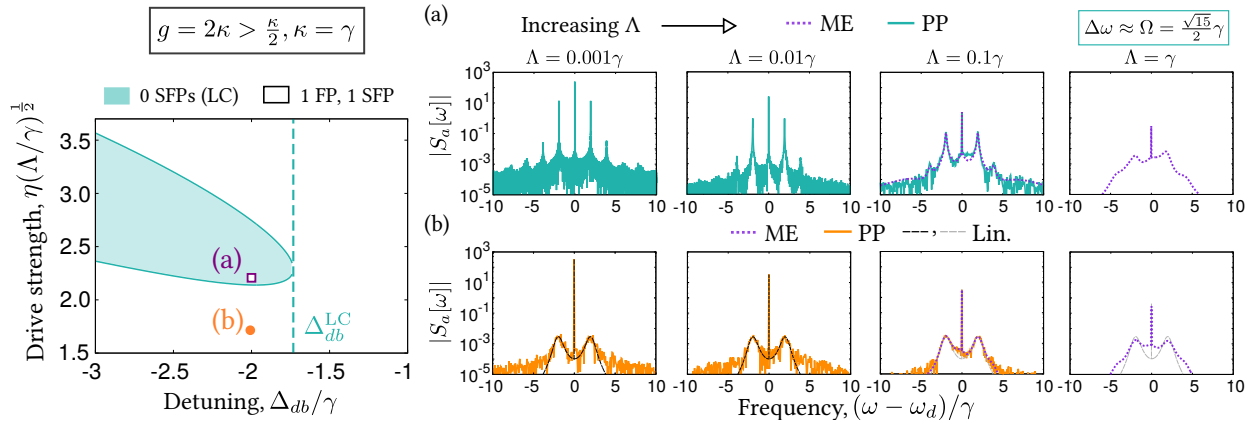


Figure 4. $|S_a[\omega]|$, logscale, (a) within, and (b) outside the **limit cycle region**, as a function of increasing nonlinearity Λ from left to right. Master equation (ME), SDE simulations (PP), and stable regime linearized spectra (Lin.) are shown.

classical drift term unchanged as discussed earlier, but scales the stochastic term by a $\frac{1}{\sqrt{c}}$ factor [45]. Hence decreasing Λ ($c > 1$; equivalently, increasing mode occupation) suppresses the relative impact of quantum dynamics, moving the system closer to effectively classical evolution.

By varying Λ and η according to the above scaling, we can stay on *fixed* positions on the *classical* phase diagram (a) just within the limit cycle region, and (b) just outside [See Fig. 4], while modifying the stochastic dynamics. For regimes of weak nonlinearity relative to the damping rates, $\Lambda \sim [0.001, 0.1]\gamma, \kappa$, we find that Eqs. (4) may be simulated controllably; here, modal occupations of $O([10^2, 10^3])$ make Master equation and even Monte Carlo simulations unfeasible. For stronger nonlinearities $\Lambda \gtrsim \gamma$, P representation SDE simulations run into notorious difficulties [49, 50]; however, weaker excitation numbers then render density matrix simulations tractable again [51]. Combining the two methods yields a complete picture of dynamics as the nonlinearity is increased to the quantum regime. The precise scaling of stochastic terms with nonlinearity does depend on the nonlinear model employed [43, 52, 53]; **more generally, our analysis may be regarded as a study of dynamics under transition from high to low modal occupations.** We analyze again the linear mode power spectrum, using the Wiener-Khinchin theorem: $S_a[\omega] = \int_{-\infty}^{\infty} d\tau e^{-i\omega\tau} \langle \hat{a}^\dagger(\tau)\hat{a}(0) \rangle$. For SDE simulations, the required correlation function is determined via averaging, $\langle \hat{a}^\dagger(\tau)\hat{a}(0) \rangle = \lim_{t \rightarrow \infty} \frac{1}{N_s} \sum_{i=1}^{N_s} \alpha_i^\dagger(t + \tau)\alpha_i(t)$, summing over at least $N_s = 10^5$ trajectories for each calculation.

Within the limit cycle region [Fig. 4 (a)], for the weakest nonlinearity $\Lambda = 0.001\gamma$, the spectrum appears close to the classical result [Fig. 3 (c)]. However, as the nonlinearity becomes stronger, the peaks in the discrete spectrum broaden.

A weak-noise phase dynamics analysis [45] indicates a phase diffusion time $\propto 1/\Lambda$ (equivalently, comb peak linewidths $\propto \Lambda$), with a proportionality coefficient of order one determined by local properties of the limit cycle attractor. Outside the unstable region [Fig. 4 (b)], the classical FP with mode occupations ($|\bar{\alpha}|^2, |\bar{\beta}|^2$) is stable. Fluctuations around this FP yield a quantum spectrum that we determine analytically [45] using a linearized analysis [46, 48, 54]; the result agrees well with $S_a[\omega]$ for weak nonlinearities, but deviates as Λ increases and the fluctuations are no longer small relative to ($|\bar{\alpha}|^2, |\bar{\beta}|^2$). For intermediate $\Lambda = 0.1\gamma$, we are able to compare SDE and Master equation simulations in both regions, finding very good agreement.

Conclusion - The driven, *strongly-coupled* nonlinear system of a Kerr oscillator and a linear mode admits a phase with no classical SFPs. Here, classical dynamics feature limit cycles with sharp peaks in the mode spectra; however, the *quantum* dynamics introduce dephasing due to the very nonlinearity that gives birth to the limit cycles, broadening and ultimately washing out these spectral peaks as Λ increases, even if all other noise sources are absent. Our study is relevant for on-chip microwave domain frequency comb generation using quantum circuits with weak nonlinearities (realized in recent circuit QED experiments [18, 55, 56]), and for further understanding stable operating regimes of JJ-based nonlinear multimode circuit QED systems.

We would like to thank Howard J. Carmichael and Mike Metcalfe for useful discussions. This work was supported by the US Department of Energy, Office of Basic Energy Sciences, Division of Materials Sciences and Engineering under Award No. DE-SC0016011.

[1] J. Clarke and F. K. Wilhelm, *Nature* **453**, 1031 (2008).

[2] P. Bertet, F. R. Ong, M. Boissonneault, A. Bolduc, F. Mallet, A. C. Doherty, A. Blais, D. Vion, and D. Esteve, [arXiv:1111.0501](https://arxiv.org/abs/1111.0501) [quant-ph] (2011), arXiv: 1111.0501.

- [3] M. H. Devoret and R. J. Schoelkopf, *Science* **339**, 1169 (2013).
- [4] A. Blais, R.-S. Huang, A. Wallraff, S. M. Girvin, and R. J. Schoelkopf, *Phys. Rev. A* **69**, 062320 (2004).
- [5] A. Wallraff, D. I. Schuster, A. Blais, L. Frunzio, R.-S. Huang, J. Majer, S. Kumar, S. M. Girvin, and R. J. Schoelkopf, *Nature* **431**, 162 (2004).
- [6] J. Majer, J. M. Chow, J. M. Gambetta, J. Koch, B. R. Johnson, J. A. Schreier, L. Frunzio, D. I. Schuster, A. A. Houck, A. Wallraff, A. Blais, M. H. Devoret, S. M. Girvin, and R. J. Schoelkopf, *Nature* **449**, 443 (2007).
- [7] L. DiCarlo, J. M. Chow, J. M. Gambetta, L. S. Bishop, B. R. Johnson, D. I. Schuster, J. Majer, A. Blais, L. Frunzio, S. M. Girvin, and R. J. Schoelkopf, *Nature* **460**, 240 (2009).
- [8] D. I. Schuster, A. Wallraff, A. Blais, L. Frunzio, R.-S. Huang, J. Majer, S. M. Girvin, and R. J. Schoelkopf, *Phys. Rev. Lett.* **94**, 123602 (2005).
- [9] J. Gambetta, A. Blais, D. I. Schuster, A. Wallraff, L. Frunzio, J. Majer, M. H. Devoret, S. M. Girvin, and R. J. Schoelkopf, *Phys. Rev. A* **74**, 042318 (2006).
- [10] L. S. Bishop, E. Ginossar, and S. M. Girvin, *Phys. Rev. Lett.* **105**, 100505 (2010).
- [11] N. M. Sundaesan, Y. Liu, D. Sadri, L. J. Szócs, D. L. Underwood, M. Malekakhlagh, H. E. Türeci, and A. A. Houck, *Phys. Rev. X* **5**, 021035 (2015).
- [12] M. D. Reed, L. DiCarlo, B. R. Johnson, L. Sun, D. I. Schuster, L. Frunzio, and R. J. Schoelkopf, *Phys. Rev. Lett.* **105**, 173601 (2010).
- [13] R. Vijay, M. H. Devoret, and I. Siddiqi, *Review of Scientific Instruments* **80**, 111101 (2009).
- [14] F. Mallet, F. R. Ong, A. Palacios-Laloy, F. Nguyen, P. Bertet, D. Vion, and D. Esteve, *Nat Phys* **5**, 791 (2009).
- [15] B. Yurke, L. R. Corruccini, P. G. Kaminsky, L. W. Rupp, A. D. Smith, A. H. Silver, R. W. Simon, and E. A. Whittaker, *Phys. Rev. A* **39**, 2519 (1989).
- [16] M. A. Castellanos-Beltran and K. W. Lehnert, *Appl. Phys. Lett.* **91**, 083509 (2007).
- [17] B. Abdo, K. Sliwa, L. Frunzio, and M. Devoret, *Phys. Rev. X* **3**, 031001 (2013).
- [18] C. Eichler, Y. Salathe, J. Mlynek, S. Schmidt, and A. Wallraff, *Phys. Rev. Lett.* **113**, 110502 (2014).
- [19] C. Macklin, K. O'Brien, D. Hover, M. E. Schwartz, V. Bolkhovskoy, X. Zhang, W. D. Oliver, and I. Siddiqi, *Science* **350**, 307 (2015).
- [20] J. M. Fink, A. Dombi, A. Vukics, A. Wallraff, and P. Domokos, *Phys. Rev. X* **7**, 011012 (2017).
- [21] M. Fitzpatrick, N. M. Sundaesan, A. C. Y. Li, J. Koch, and A. A. Houck, *Phys. Rev. X* **7**, 011016 (2017).
- [22] M. Boissonneault, J. M. Gambetta, and A. Blais, *Phys. Rev. Lett.* **105**, 100504 (2010).
- [23] M. I. Dykman and M. A. Krivogla, *Soviet Journal of Experimental and Theoretical Physics* **50**, 30 (1979).
- [24] I. Siddiqi, R. Vijay, F. Pierre, C. M. Wilson, M. Metcalfe, C. Rigetti, L. Frunzio, and M. H. Devoret, *Phys. Rev. Lett.* **93**, 207002 (2004).
- [25] I. Siddiqi, R. Vijay, F. Pierre, C. M. Wilson, L. Frunzio, M. Metcalfe, C. Rigetti, R. J. Schoelkopf, M. H. Devoret, D. Vion, and D. Esteve, *Phys. Rev. Lett.* **94**, 027005 (2005).
- [26] M. Dykman, *Fluctuating Nonlinear Oscillators: From Nanomechanics to Quantum Superconducting Circuits* (OUP Oxford, 2012).
- [27] P. Del'Haye, A. Schliesser, O. Arcizet, T. Wilken, R. Holzwarth, and T. J. Kippenberg, *Nature* **450**, 1214 (2007).
- [28] P. Del'Haye, O. Arcizet, A. Schliesser, R. Holzwarth, and T. J. Kippenberg, *Phys. Rev. Lett.* **101**, 053903 (2008).
- [29] J. S. Levy, A. Gondarenko, M. A. Foster, A. C. Turner-Foster, A. L. Gaeta, and M. Lipson, *Nat Photon* **4**, 37 (2010).
- [30] T. Herr, V. Brasch, J. D. Jost, C. Y. Wang, N. M. Kondratiev, M. L. Gorodetsky, and T. J. Kippenberg, *Nat Photon* **8**, 145 (2014).
- [31] R. P. Erickson, M. R. Vissers, M. Sandberg, S. R. Jefferts, and D. P. Pappas, *Phys. Rev. Lett.* **113**, 187002 (2014).
- [32] H. A. Haus, *IEEE Journal of Selected Topics in Quantum Electronics* **6**, 1173 (2000).
- [33] J. Faist, G. Villares, G. Scalari, M. Rösch, C. Bonzon, A. Hugi, and M. Beck, *Nanophotonics* **5** (2016), 10.1515/nanoph-2016-0015.
- [34] A. Ganesan, C. Do, and A. Seshia, *Appl. Phys. Lett.* **111**, 064101 (2017).
- [35] A. Ganesan, C. Do, and A. Seshia, *Phys. Rev. Lett.* **118**, 033903 (2017).
- [36] Y. K. Chembo and N. Yu, *Phys. Rev. A* **82**, 033801 (2010).
- [37] T. S. Mansuripur, C. Vernet, P. Chevalier, G. Aoust, B. Schwarz, F. Xie, C. Caneau, K. Lascola, C.-e. Zah, D. P. Caffey, T. Day, L. J. Missaggia, M. K. Connors, C. A. Wang, A. Belyanin, and F. Capasso, *Phys. Rev. A* **94**, 063807 (2016).
- [38] K. Rayanov, B. L. Altshuler, Y. G. Rubo, and S. Flach, *Phys. Rev. Lett.* **114**, 193901 (2015).
- [39] B. v. d. P. J. D. Sc., *The London, Edinburgh, and Dublin Philosophical Magazine and Journal of Science* **2**, 978 (1926).
- [40] S. H. Strogatz, *Nonlinear Dynamics and Chaos: With Applications to Physics, Biology, Chemistry, and Engineering* (Avalon Publishing, 1994) google-Books-ID: FIYHiBLWCJMC.
- [41] S. Louca, [arXiv:1506.00756 \[math\]](https://arxiv.org/abs/1506.00756) (2015), arXiv: 1506.00756.
- [42] N. Lörch, J. Qian, A. Clerk, F. Marquardt, and K. Hammerer, *Phys. Rev. X* **4**, 011015 (2014).
- [43] C. Navarrete-Benlloch, T. Weiss, S. Walter, and G. J. de Valcárcel, *Phys. Rev. Lett.* **119**, 133601 (2017).
- [44] J. Bourassa, F. Beaudoin, J. M. Gambetta, and A. Blais, *Phys. Rev. A* **86**, 013814 (2012).
- [45] See Supplementary Material [url], which includes Ref. [57].
- [46] P. D. Drummond and D. F. Walls, *J. Phys. A: Math. Gen.* **13**, 725 (1980).
- [47] M. P. da Silva, D. Bozyigit, A. Wallraff, and A. Blais, *Phys. Rev. A* **82**, 043804 (2010).
- [48] H. J. Carmichael, *Statistical Methods in Quantum Optics 1 - Master | Howard J. Carmichael | Springer* (2002).
- [49] A. Gilchrist, C. W. Gardiner, and P. D. Drummond, *Phys. Rev. A* **55**, 3014 (1997).
- [50] C. Gardiner, *Quantum Noise - A Handbook of Markovian and Non-Markovian | Crispin Gardiner | Springer* (2004).
- [51] J. R. Johansson, P. D. Nation, and F. Nori, *Computer Physics Communications* **184**, 1234 (2013).
- [52] A. Kamal, A. Marblestone, and M. Devoret, *Phys. Rev. B* **79**, 184301 (2009).
- [53] W. Casteels and C. Ciuti, *Phys. Rev. A* **95**, 013812 (2017).
- [54] S. Chaturvedi, C. W. Gardiner, I. S. Matheson, and D. F. Walls, *J Stat Phys* **17**, 469 (1977).
- [55] C. Eichler and A. Wallraff, *EPJ Quantum Technology* **1**, 2 (2014).
- [56] X. Zhou, V. Schmitt, P. Bertet, D. Vion, W. Wustmann, V. Shumeiko, and D. Esteve, *Phys. Rev. B* **89**, 214517 (2014).

- [57] S. M. Girvin, in [Quantum Machines: Measurement and Control of Engineered Quantum Systems](#) (Oxford University Press, 2014) pp. 113–256, doi: 10.1093/acprof:oso/9780199681181.003.0003.